Supporting information for:

Vapor-Based Interferometric Measurement of Local Evaporation Rate and Interfacial Temperature of Evaporating Droplets (Published in Langmuir 2014)

Sam Dehaeck, Alexey Rednikov and Pierre Colinet*

Transfers, Interfaces and Processes (TIPs), Université Libre de Bruxelles (ULB), Av. F.D. Roosevelt 50, 1050 Brussels, Belgium

E-mail: pcolinet@ulb.ac.be

A. More Details on the Experimental Procedure

Setup and Image Analysis

A classical Mach-Zehnder interferometer is here used to measure the vapour cloud surrounding an evaporating pendant drop of 3M™ Novec™ HFE-7000 deposited on a silicon wafer with a syringe. However, in our first experiments we observed that the droplet is highly mobile on such a perfectly flat substrate, which rendered its tracking over time impossible. To make it 'stick' to a single location we use photo-litography to deposit a small object which remains always within the droplet but still prevents the drop from moving away. This object has the shape of a disk 100 µm thick and 2 mm in diameter (noticeable in Figure S1a) made in SU-8 resin. We should stress that this protrusion has no impact on the validity of our vapour cloud measurements as it remains immersed in the drop for sufficiently large drops (see Figure S1b). If it has any effect, it will be on the recirculation inside the droplet, and even that is expected to be minor. Problems arise only for smaller drops, with a diameter approaching that of the cylindrical protrusion. As such, we decided to limit the present study to droplets larger than 2.4 mm in diameter. On the other hand, such a limitation to larger drops suited us well from the viewpoint of both a better resolution of the vapour cloud and a possible comparison with boundary-layer simulations (valid for large enough droplet sizes).

---

*To whom correspondence should be addressed

As explained in the main text, a reference image is acquired before the deposition of the drop, which is shown in Figure S1(a). Its phase is analysed for each pixel and compared to that in the presence of the droplet (see Figure S1b). This leads to a "wrapped" phase map which is shown in Figure S1(c). An unwrapping algorithm then gets rid of the discontinuities and sets the total phase jump outside of the plume equal to zero. This final phase map is shown in Figure S1(d).

Finally note that the fringes are chosen to be vertical in our measurements. While any orientation is in principle possible, the current configuration is preferred due to the fact that the Fourier transform profilometry algorithm has the side-effect of a low pass filter in the direction perpendicular to the sense of the fringes. As the concentration gradients along the interface normals are predominantly vertical, a horizontal smoothing is preferred, thus leading to the use of vertical fringes.
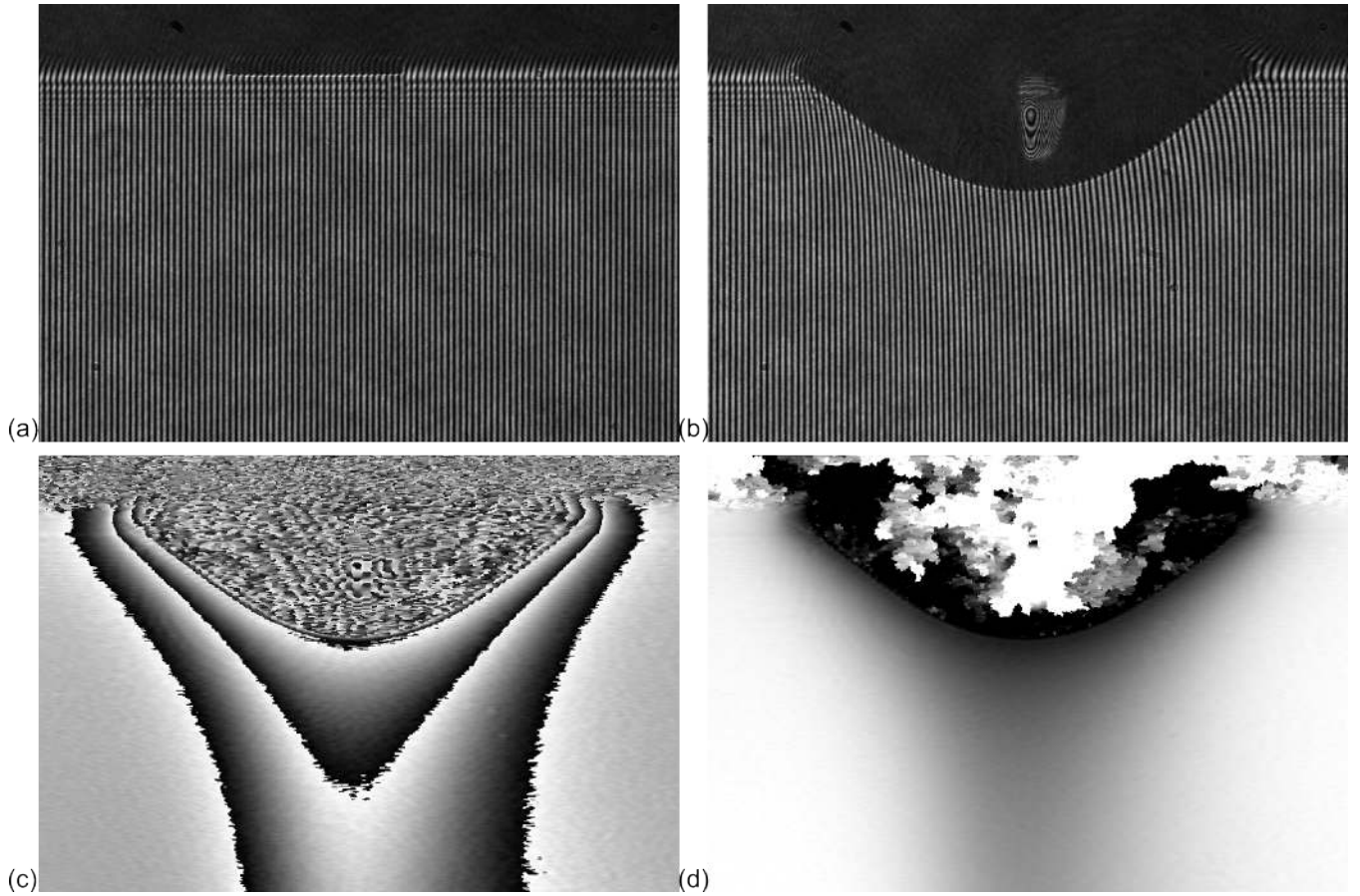

Figure S1: (a) Reference image. (b) Raw image with droplet. (c) Wrapped phase. (d) Unwrapped phase.

Tomographic Reconstruction

Given that interferometry is a line-of-sight technique, the obtained phase-shift field still needs to be tomographically reconstructed to yield the three dimensional field of the refractive index. If the target is axisymmetric, an inverse Abel transform can typically be used on a single view to obtain a meridian half-plane representation thereof[S1]. Applied to the present case, the refractive-index difference field Δn (at a given height z) is given by

$$\Delta n \left(r \right) = \frac{-\lambda}{2\pi^2} \int_r^\infty \frac{\phi'(x)}{\sqrt{x^2 - r^2}} dx \,,$$

where r is the cylindrical radial coordinate, λ is the wavelength of the laser and $\phi'(r)$ is the derivative of the phase-shift field extracted from the fringe images (as described in the previous subsection). Inherent to this transform is a certain augmentation of the noise, especially near the symmetry axis. As such, many of the algorithms proposed over the years add a certain filtering capability to alleviate these problems.[S2] We have implemented three different algorithms in order to ascertain which one could give the best results in our particular case: the three-point Abel transform method[S1], the Modified Fourier-Hankel (MFH) method[S2] and the Even-Power (EP) method[S3]. The preliminary scan of these three algorithms has shown that all methods give essentially the same results. However, with the aim of extracting local gradients, the smooth result from the EP-method is preferred for the present work.

Converting Refractive Index into Vapour Mole Fraction

After the Abel transform has yielded the refractive-index field, a conversion relation is still needed to convert this into the vapour concentration field. From the Lorentz-Lorenz equation[S4,S5], it is known that the refractive index of a mixture of gases can be expressed as

$$n_{\mathrm{mix}} - 1 = \frac{3P_{\mathrm{tot}}}{2\mathcal{R}T} \sum_i \chi_i A_i \,, \tag{1}$$

where n_{mix} is the refractive index of the mixture, P_{tot} is the total ambient pressure, $\mathcal{R}$ the universal gas constant, T the temperature, χ_i is the mole fraction of the component i and A_i is the molecular polarisability of the component i. Treating the gas as a binary mixture of air and HFE-7000 vapour, we have

$$n_{\mathrm{mix}} - 1 = \frac{3P_{\mathrm{tot}}}{2\mathcal{R}T} \left(\chi A_{\mathrm{HFE}} \right) + (1 - \chi)(n_{\mathrm{air}} - 1) \,,$$

or rather

$$n_{\mathrm{mix}} - n_{\mathrm{air}} = \frac{3P_{\mathrm{tot}}}{2\mathcal{R}T} \chi \left(A_{\mathrm{HFE}} - A_{\mathrm{air}} \right) \,,$$

or

$$n_{\mathrm{mix}} - n_{\mathrm{air}} = \chi \left(n_{\mathrm{HFE}} - n_{\mathrm{air}} \right) \,. \tag{2}$$

Thus eq 2 of the main text is recovered with n_{HFE} the refractive index of pure HFE vapour at P_{tot} and T and n_{air} is that of air. Thus, as it is experimentally the value $\Delta n = n_{\mathrm{mix}} - n_{\mathrm{air}}$ that is measured in our holographic setup (due to the phase substraction of a reference image in 'pure' air), just a proportionality constant is needed to transform the obtained refractive index profile into the mole-fraction distribution χ if the pressure and temperature are assumed constant.

To quantify this proportionality constant, only the refractive index of pure HFE-7000 vapour is needed. However, as this is not yet known it must be measured here. With no dedicated gas refractometer available, we simply measure the absolute refractive index of an atmosphere

saturated with HFE-7000 vapour at different temperatures. To this end, a square cuvette with internal dimensions of 5×5 cm is filled with a minimal amount of liquid HFE-7000 after which a cover is placed on the top to prevent further evaporation. The Δn value is measured by starting from the thereby attained saturated state just above the liquid interface (hence a known value of χ) and interferometrically following the changes in the optical path as the liquid is then allowed to progressively and completely evaporate. Thus, the proportionality constant to convert Δn into χ is found to be 737 ± 16 (i.e. $n_{\text{HFE}} = 1.00163 \pm 2.9 \times 10^{-5}$) for a wavelength of 660 nm, atmospheric pressure and 24°C. This implies a difference in the refractive index of approximately $+8.3 \times 10^{-4}$ as the relative humidity of HFE-7000 is changed from 0% to 100%. This large difference is caused by a combined effect of a substantial difference in the refractive index of pure HFE-7000 and ambient air (estimated to be 1.36×10^{-3}) and the fact that the saturation mole fraction at ambient conditions is as large as 61%. In typical ambient temperatures ranging from 20°C to 25.5°C, the current calibration procedure achieves a reasonable accuracy of around 2.17% (over 7 measurement points).

As in the experiment not only the concentration but also the gas temperature is non-uniform, it is important to assess the influence of the latter. To that end, we start from the same eq 1 but now taking into account that the refractive-index difference measured is not the same as in eq 2, but rather $\Delta n = n_{\text{mix}} - n_{\text{air,amb}}$ with n_{mix} being at a locally varying temperature. Having this end goal in mind, we now derive eq 1 of the main text, which is repeated here:

$$\chi = \frac{1}{n_{\text{HFE,amb}} - n_{\text{air,amb}}} \frac{T}{T_{\text{amb}}} \left[\Delta n - (n_{\text{air,amb}} - 1) \left(\frac{T_{\text{amb}}}{T} - 1 \right) \right] . \tag{3}$$

From this formula we can note that there are two error sources appearing if one neglects the temperature variation and simply uses eq 2. The first comes from the proportionality factor being in reality temperature-dependent. Thus, a temperature difference of 10°C will lead to an error of $\sim 3.4\%$ in the estimated χ. The second error source comes from the fact that we (holographically) compare the refractive index of the mixture with the refractive index of air measured before the start of the experiment (i.e. still at ambient temperature). The importance of this term depends on the magnitude of Δn. When assuming a mole fraction of 0.6, this error is only $\sim 1.2\%$. If the local mole fraction is 0.4, the error increases to $\sim 1.7\%$. Unfortunately, both errors work in the same direction and as $T \leq T_{\text{amb}}$, eq 2 is biased into overestimating the mole fraction by up to 5% if temperature differences of the order of 10°C eventually take place in our setup.

Interface Contour Extraction

For obvious reasons, it is necessary to localise the droplet interface on the interferometric image. As the interferometric fringes render this difficult, in a first step the fringes are eliminated by taking the amplitude of the complex intensity image generated in the Fourier transform profilometry algorithm but disregarding its phase. This image is then thresholded and from the resulting image, the contour of the drop is extracted. The obtained points are fitted with a fourth-order polynomial (as this allows to account for the gravity-induced shape deformation) to yield a smooth contour. As it is visible in Figure S2, a good fitting is obtained. The obtained shape is used to track the droplet volume over time and thus to provide an independent measurement of the global evaporation rate of the droplet.
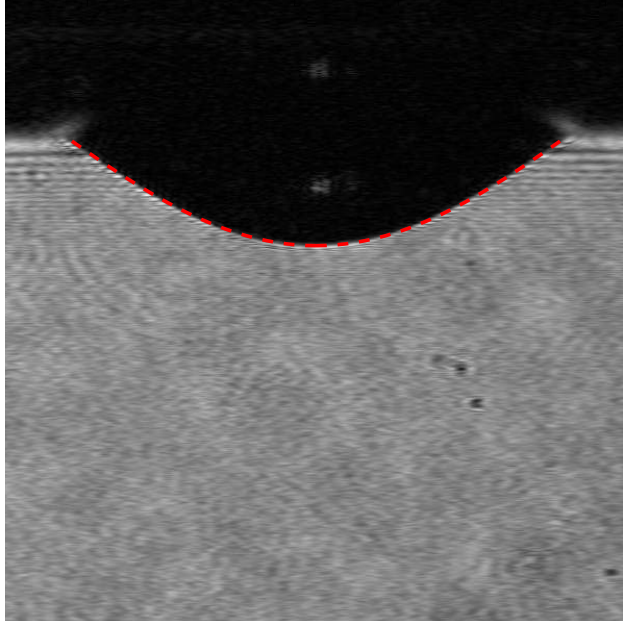
Figure S2: After removal of the fringes from the interferometric image, a satisfactory contour fit can be found using a fourth-order polynomial.

Interfacial Temperatures

Knowing the interface location, it is straightforward to determine the normals to it. The refractive-index difference along these lines can then be extracted from the refractive-index difference map through bilinear interpolation. A more precise estimation of the interfacial refractive-index difference is obtained from a quadratic fit over 560 µm starting from 35 µm from the interface. There are now two ways to obtain an estimate for the interfacial temperature from this refractive index difference (as explained in the main text). One can simply use the proportionality relation given by eq 2 and use this value χ_σ inside $\chi_\sigma = P_{\mathrm{sat}}(T_\sigma)/P_{\mathrm{amb}}$ with P_{sat} provided by 3M™. However, as mentioned above, local temperature non-uniformities influence the measured refractive-index field leading to a general overestimation by a few percent of the local mole fraction when using eq 2. A more accurate way is to use the measured interfacial refractive index inside eq 3 combined with $\chi_\sigma = P_{\mathrm{sat}}(T_\sigma)/P_{\mathrm{amb}}$ and solve for both unknowns at the same time. A comparison of the uncorrected (first method) and corrected (second method) measured interfacial temperature distributions is shown in Figure S3. Here one can clearly see that the correction is more essential for larger differences with the ambient temperature (24°C). This corrected interfacial temperature (or more specifically χ_σ) is used in the local-evaporation-rate determination (cf. eq 3 in the main text and eq 5 below). However, without assuming some sort of temperature profile surrounding the drop, it is impossible to apply a similar correction to the local-concentration-gradient determination (the latter is realised based on eq 2 and not on eq 3). Yet, as the temperature boundary layer must be thicker than the concentration layer (the diffusion coefficient is smaller than the thermal diffusivity), the error on the concentration gradient must be even smaller than on the absolute values (i.e. <5%).

Finally, note that it is not the raw measurements for χ_σ (and T_σ) that are used in the numerical simulations described below but rather the following smoothed result based on the fitting formula

$$\chi_\sigma = \alpha + (0.61 - \alpha)\, e^{\beta(r^\gamma - 1)}, \tag{4}$$
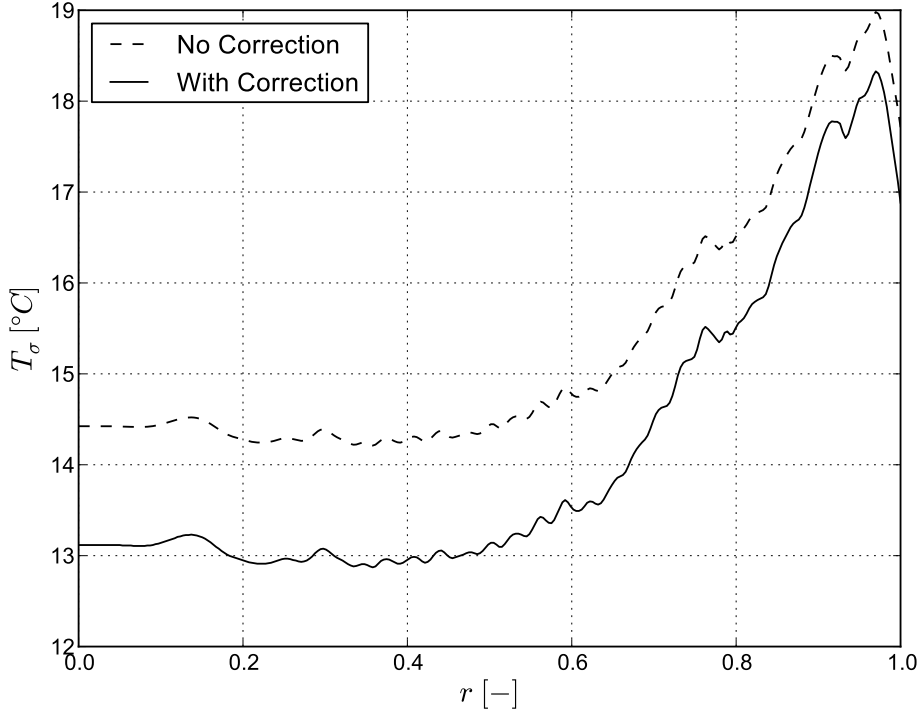
Figure S3: The role of correcting for temperature effects in the refractive-index conversion on measured interfacial profiles.

which recovers the ambient temperature at the contact line (i.e. $\chi_\sigma = 0.61$) and at the same time captures reasonably well the experimental data (cf. the solid line in Figure 4 of the main text). The obtained fitting parameters α, β and γ are specified later on.

Local Evaporation Rate Determination

From the normal profiles, the gradient can now be extracted at the interface. However, as central differencing gives a noisy result, a linear fit is performed over 185 µm starting from 35 µm from the interface and its gradient is used. Applying the following formula then yields the distribution of the local evaporation rate $J_{l,Exp}$ along the droplet interface:

$$J_{l,Exp} = -\frac{M_v P_{\text{tot}} D_v}{\mathcal{R}T\left(1 - \chi_\sigma\right)}\left.\frac{\partial \chi}{\partial n}\right|_\sigma \tag{5}$$

with M_v the molar weight of the vapour ($0.2\,\text{kg/mol}$), P_{tot} the total (atmospheric) pressure, D_v the diffusion coefficient of the vapour–air mixture ($8.11 \times 10^{-6}\,\text{m}^2/\text{s}$) obtained by independent Stefan-tube experiments, $\mathcal{R}$ the universal gas constant ($8.31\,\text{J/mol\,K}$), T the temperature, χ_σ the mole fraction at the interface (see above) and $\left.\frac{\partial \chi}{\partial n}\right|_\sigma$ the normal mole-fraction gradient at the interface. As spatial variations of the gas pressure are expected to be thermodynamically negligible, we take $P_{\text{tot}} = P_{\text{amb}}$. On the other hand, given that the corresponding effect is anyway not taken into account e.g. in the refractive-index calibration away from the interface, it is consistent to set $T = T_{\text{amb}}$ in eq 5 too and to evaluate D_v just at T_{amb}. In this way, we recover eq 3 of the main text.

Global Evaporation Rates

Determination from Interfacial Gradients

Another quantity that can be extracted from the vapour interferometer is the global evaporation rate of the drop. There are several ways in which this can be accomplished. The easiest one is to integrate the obtained local evaporation rates $J_{l,Exp}$ over the surface of the drop. Thus, the following integration is performed with h' the radial derivative of the local thickness of the drop and R_c its contact radius:

$$J_{g,surf} = \int_0^{R_c} 2\pi r \sqrt{1 + h'^2} J_{l,Exp} dr \,, \tag{6}$$

where all variables are dimensional.

Determination from Iso-Concentration Lines

As the normal gradient at the contact line is eventually infinite and because the profile fitting of the drop is subject to some uncertainty, a second method, using the iso-concentration lines, was also developed to avoid this source of imprecision.

The vapour mole flux $\vec{j}_v^*$ [mol/m^{2}s] at any point in the gas is related to the total mole flux $\vec{j}^*$ by

$$\vec{j}_v^* = \chi \vec{j}^* - n_g D_v \vec{\nabla} \chi \,, \tag{7}$$

with $n_g = \frac{P_{\text{amb}}}{\mathcal{R} T_{\text{amb}}}$ the gas mole density and the asterisk serving to distinguish the mole fluxes from the corresponding mass ones (the latter without asterisk). At the droplet interface, neglecting air absorption (i.e. no air flux) as well as the interface digression velocity versus the gas velocity, we have

$$\vec{j}_v^* \cdot \vec{n}\Big|_\sigma = \vec{j}^* \cdot \vec{n}\Big|_\sigma = J_l / M_v \,, \tag{8}$$

from where eq 3 of the main text can be recovered on account of eq 7. Hereafter $\vec{n}$ is the external (pointing away from the droplet) unit normal to a surface considered.

The global evaporation flux from the droplet can be calculated as

$$J_g^* = \int \vec{j}_v^* \cdot \vec{n} \, dS = \int \vec{j}^* \cdot \vec{n} \, dS \,, \tag{9}$$

where the integration can be performed over any surface encompassing the droplet and ending on the substrate. The second equality of eq 9 follows from neglecting the same factors as for eq 8 and in addition assuming quasi-stationarity of the mole-fraction field, all which means that the amount of air remains unchanged in the encompassed region. Note that this integral equality takes place in spite of generally $\vec{j}_v^* \cdot \vec{n} \neq \vec{j}^* \cdot \vec{n}$. Obviously, the droplet interface itself can in particular be used in eq 9, which then coincides with eq 4 of the main text on account of eq 8 and $J_g^* = J_g / M_v$. Otherwise, eq 9 does not seem to be very practical, as there is no way to infer $\vec{j}_v^*$ or $\vec{j}^*$ from the measured mole-fraction field (eq 7 is not enough to this purpose) without simultaneously measuring the velocity field, which we do not do here. However, if the integration in eq 9 is performed over an iso-concentration surface, $\chi = $ const, further progress can be made just with what we already

have. Indeed, using eq 7 in eq 9 and taking $\chi = \mathrm{const}$ out of the integral, one can deduce

$$J_g^* = \chi\, J_g^* - \int_{\chi=\mathrm{const}} n_g D_v \frac{\partial \chi}{\partial n}\, dS\,,\tag{10}$$

which on account of $n_g = \frac{P_{\mathrm{amb}}}{\mathcal{R} T_{\mathrm{amb}}}$ and $J_g^* = J_g/M_v$ yields eq 5 of the main text.

Thus, the integration over the isocontours provides yet another method for the determination of the global evaporation rate J_g just on the basis of the measured mole-fraction field. The result is denoted as $J_{g,iso}$, as already mentioned in the main text.
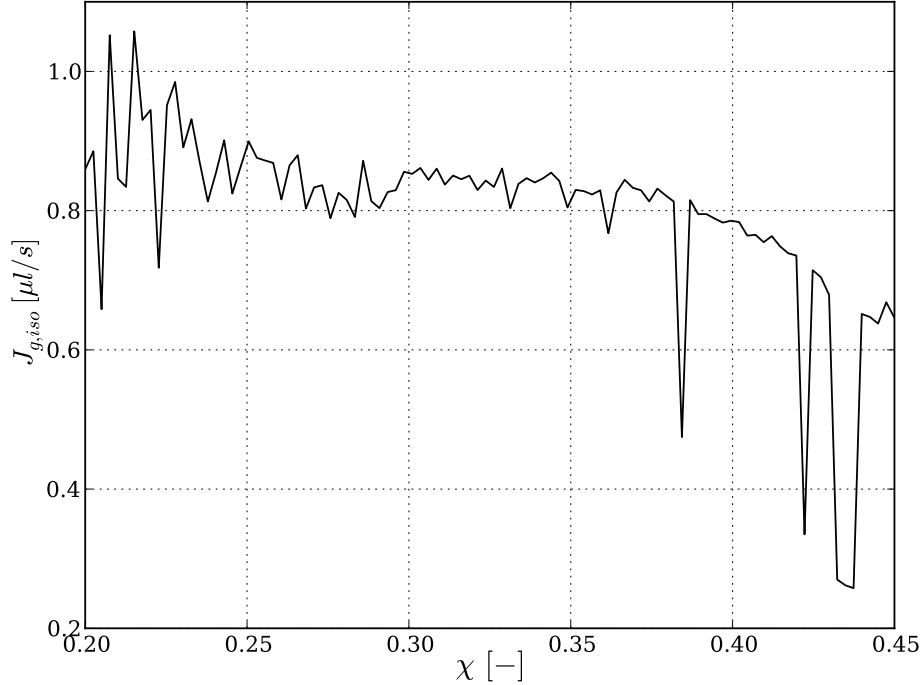

Figure S4: Global evaporation rate versus iso-concentration values along which it is calculated by means of eq 10.

The advantage of this second method is clearly the fact that the global evaporation rate can be obtained on any isocontour, which permits to average the measurement over multiple isocontours to get a more accurate global evaporation rate, as well as to estimate what is the accuracy of the measurement. Note that the assumption of a quasi-stationary concentration field could pose a problem in some cases. In Figure S4, the global evaporation rate $J_{g,iso}$ calculated in this way is shown versus the mole fraction χ of the isocontour. This shows that it is relatively constant for χ between 0.25 and 0.35. Indeed, checking the iso-concentration lines in a treated image, contours for lower χ tend to become erratic (due to noise), whereas larger χ tend not to encompass the entire droplet interface (due to the interface cooling and the corresponding decrease of the interfacial mole fraction). Note that the uncertainty (95% confidence interval) on the global evaporation rate based on a single instantaneous image in this range (for χ between 0.25 to 0.35) is only $\pm 6\%$.

B. Performance of the Inverse Abel Transform in the Presence of Singularities

In the case of a purely diffusion-limited evaporation regime, theory predicts that the mole fraction field is non-differentiable near the contact line (but remains continuous). In order to assess whether the inverse Abel transform is capable of correctly reconstructing such a field, a numerical experiment was performed. From theory[S6], the following analytical formula for the mole-fraction field χ can be obtained in the limit of pure diffusion for a flattened drop with a given constant interfacial mole fraction χ_σ:

$$\chi(r,z) = \frac{2\chi_\sigma}{\pi}\left(\frac{\pi}{2} - \arctan\left(\sqrt{\frac{\sqrt{(1-z^2-r^2)^2 + 4z^2} - (1-z^2-r^2)}{2}}\right)\right). \tag{11}$$

The next step is to transform this mole-fraction field into a simulated interferometric image. To this end, it is multiplied by $n_{\text{HFE}} - n_{\text{air}}$ to convert it into the local refractive index (see eq 2) and it is then integrated along a line of sight (in y-direction) and converted into a phase delay $\Delta\phi$. Note that an artificially large but finite cut-off value y_c was used as the concentration field decays (too) slowly for the Abel transform. The choice of this cut-off value was shown to not influence the presented results. This is obtained through the following formula:

$$\Delta\phi = \frac{4\pi}{\lambda}\int_{-y_c}^{y_c} \chi\left(n_{\text{HFE}} - n_{\text{air}}\right) dy. \tag{12}$$

The cosine of this phase field is then shown in the inset of Figure S5. This phase image is then subjected to an inverse Abel transform treatment similar to the one used for the experimental images. The extracted mole fraction along a vertical line starting at the contact line is compared to the original theoretical result in Figure S5. This shows that the reconstruction is accurate over the main portion of the field. However, close to the interface, the gradient becomes too large and an underprediction of both the interfacial concentration and the interfacial gradient is an inevitable result. Note that unfortunately exactly the same inversion algorithm as in the experiment could not be used here as the EP-method does not work for the inversion of phase images that do not drop smoothly to zero at the edge of the image. As a result, the MFH algorithm[S2] was used as a model algorithm here. The effect is expected to be similar for the EP method, as both algorithms give similar local evaporation rates and interfacial temperatures when applied to the experimental results.

So, from the fundamental point of view, many Abel inversion algorithms (such as the ones we have used) are not capable of returning an infinite local evaporation rate at the contact line. On top of this there is also the additional smoothing described above, where a local fitting close to the interface is extrapolated to obtain a smoother value of the gradient at the droplet interface. Needless to say that this smoothing also prevents obtaining an infinite concentration gradient at the contact line.
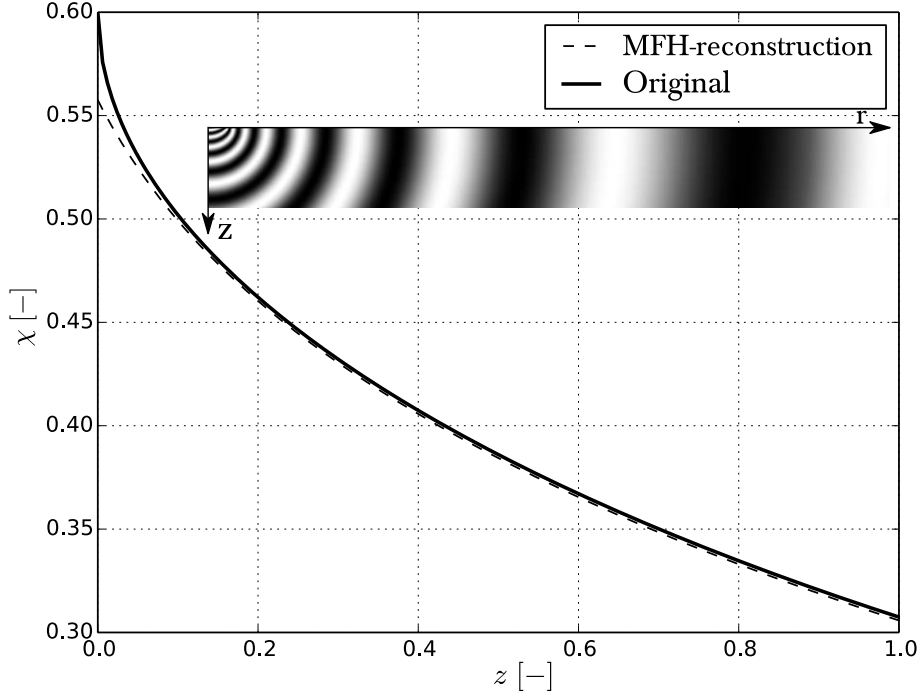
Figure S5: Simulated phase image and reconstructed mole-fraction profiles.

C. More Details on the Numerical Simulations

Pure-Diffusion Reference Case

To compare the measured vapour cloud shape and the measured local and global evaporation rates to the purely-diffusive reference case, an axisymmetric numerical simulation is performed with OpenFOAM 2.1 (more specifically LaplacianFoam) for solving $\nabla^2 \chi = 0$. For the computational domain, an arc of a circle fitted to the experimental drop contour is used as a constant-mole-fraction boundary on which $\chi = \chi_\sigma = P_{\text{sat}}\left(T_{\text{sat}}\right)/P_{\text{amb}} = 0.61$, while a circular domain 10 times larger than the drop contact radius is used as an external boundary, on which $\chi = 0$ is imposed (no vapour in ambient). A linear grid refinement is applied in both the radial and vertical directions in order to better resolve the near-contact-line region. This turns out not to be enough to properly resolve the singularity of the local evaporation rate at the contact line though, but as this simulation is only used for plotting the overall vapour cloud configuration, the issue is not pushed further.

Formulas found in the literature[S6] are rather used for plotting the local and global evaporation rates. As no agreement is expected anyway with the pure-diffusion regime for the present experiments, and as we are merely interested in contrasting the corresponding results, we shall limit ourselves to the flattened-drop formulas. For the local evaporation rate $J_{l,D}$ as a function of the (dimensional) radial coordinate r, we have[S6]

$$J_{l,D}(r) = \frac{2D_v \rho_{v,\sigma}}{\pi \sqrt{R_c^2 - r^2}}. \tag{13}$$

Here, D_v is the diffusion coefficient of the vapour in air, R_c is the contact radius of the drop and $\rho_{v,\sigma} = \frac{P_{\text{amb}}}{\mathcal{R}T_{\text{amb}}} M_v \chi_\sigma$ is the vapour density at the interface, assumed constant when deriving eq 13. It is important to stress that eq 13 is obtained under the assumption that the vapour fraction is small and therefore the convective effect of Stefan flow can be neglected. This is also done tacitly in the

mentioned numerical simulation as $\nabla^2 \chi = 0$ is only valid when no such convective contribution is involved. However, in our present setup, it is by no means negligible as the mole fractions are of the order of 60%. This has not been rigorously implemented in the calculations but to nevertheless get a feeling for the impact this could have on the evaporation rate, the following Stefan-Fuchs correction[S7] to the local evaporation rate is used:

$$J_{l,DSF}(r) = \frac{J_{l,D}(r)}{1 - \chi_\sigma}. \tag{14}$$

This is believed to overestimate the evaporation rate, as the ignored convective effect of Stefan flow will itself generally tend to decrease the mole-fraction gradients at the droplet interface. The global evaporation rate can be obtained by integrating the local evaporation rate over the entire droplet interface, which, for flattened drops, evaluates to

$$
\begin{aligned}
J_{g,D} &= 4 D_v \rho_{v,\sigma} R_c, \tag{15} \\
J_{g,DSF} &= \frac{4 D_v \rho_{v,\sigma} R_c}{1 - \chi_\sigma}. \tag{16}
\end{aligned}
$$

Large-Grashof-number limit: boundary-layer approach

Assumptions and dimensionless numbers

As evidenced by the experimental results, solutal (density variation with the vapour concentration) buoyancy convection in the gas phase must play an important role in the studied phenomenon, all the more so that we are here dealing with a highly volatile liquid (HFE-7000) with a large molecular weight ($M_v = 0.2\,\text{kg/m}^3$). It totally reshapes the vapour cloud as compared to the pure-diffusion case and thus essentially affects the evaporation rates. The intensity of this convective effect is characterised by a Grashof number Gr, which we can here define as

$$Gr = \frac{\Delta \rho_g g R_c^3}{\mu_{\text{air}} \nu_{\text{air}}}, \tag{17}$$

where $\Delta \rho_g$ is the scale of the gas density variation, g is the gravity acceleration, R_c is the contact radius of the pendant drop, $\mu_{\text{air}} = 1.85 \times 10^{-5}\,\text{Pa}\,\text{s}$ is the dynamic viscosity of pure air, and $\nu_{\text{air}} = 1.58 \times 10^{-5}\,\text{m}^2/\text{s}$ its kinematic viscosity. Now the pure-diffusion limit (which, on account of essential vapour mole fractions, is understood in this section as inherently incorporating the associated Stefan flow) actually corresponds to $Gr \ll 1$, which is obviously not the case in the present experiments. Note that the Schmidt number is here of order unity ($Sc = \nu_{\text{air}}/D_v = 1.95$ with $D_v = 0.811 \times 10^{-5}\,\text{m}^2/\text{s}$ the diffusion coefficient[S8]), which permits asymptotic characterisation of the phenomenon solely in terms of Gr. Let us now estimate the values of $\Delta \rho_g$ and Gr for our problem, and make a number of other useful developments in passing.

If χ is the mole fraction of vapour in the gas phase, the gas density ρ_g can be expressed as $\rho_g = c_g [M_{\text{air}} + (M_v - M_{\text{air}})\chi]$, where c_g is the mole density of the gas and $M_{\text{air}} = 0.029\,\text{kg/mol}$. In what follows, we shall neglect the temperature dependence of all properties (the expected temperature differences must here be much smaller than the absolute temperature) and use their values at a temperature of $\sim 25°C$. This is done except for the saturation conditions, where the temperature dependence is especially strong and essential. We shall also treat the gas as ideal. Besides, any hydrodynamic and hydrostatic pressure variation must here be small against the absolute pressure

value. In this way, in particular, $c_g \approx \text{const} = P_{\text{amb}}/\mathcal{R}T_{\text{amb}}$, where $\mathcal{R}$ is the universal gas constant and P_{amb} and T_{amb} are the ambient pressure and temperature, and $\rho_{\text{air}} \approx c_g M_{\text{air}}$ is the density of pure air under the same ambient conditions ($\chi \to 0$ and $\rho_g \to \rho_{\text{air}}$ far away from the droplet). If $P_{\text{sat}}(T)$ is the saturation pressure (here of HFE-7000) as a function of temperature, for which we here use the Clausius-Clapeyron relation $P_{\text{sat}}(T) = P_{\text{sat}}(T_0) \exp\left[L\,M_v(T - T_0)/\mathcal{R}TT_0\right]$ with L being the latent heat of evaporation (in J/kg), the corresponding saturation mole fraction is $\chi_{\text{sat}}(T) = P_{\text{sat}}(T)/P_{\text{amb}}$. The maximum value of χ_{sat} is attained at the contact line, where the temperature is practically the ambient one, and decreases towards the center of the drop (Figure 4 of the main text). We shall define $\Delta\rho_g$ as the difference between the maximum value of ρ_g (in view of $M_v > M_{\text{air}}$, attained at the contact line too) and ρ_{air}. Thus,

$$\Delta\rho_g = \rho_{g,\text{max}} - \rho_{\text{air}} = \frac{P_{\text{amb}}}{\mathcal{R}T_{\text{amb}}}\left(M_v - M_{\text{air}}\right)\chi_{\text{sat}}(T_{\text{amb}}) = \frac{P_{\text{sat}}(T_{\text{amb}})}{\mathcal{R}T_{\text{amb}}}\left(M_v - M_{\text{air}}\right). \tag{18}$$

With $L = 142\,\text{kJ/kg}$, $T_{\text{amb}} = 297.15\,\text{K}$, $P_{\text{sat}}(T_{\text{amb}}) = 62.2\,\text{kPa}$, one obtains $\Delta\rho_g = 4.31\,\text{kg/m}^3$, which is several times larger than the density of pure air, $\rho_{\text{air}} = 1.18\,\text{kg/m}^3$, at $P_{\text{amb}} = 1\,\text{atm}$.

Then, for a drop of $R_c = 1.81\,\text{mm}$, it follows from eq 17 that Gr is as large as 852, which goes well along with the observed concentration fields being far from the pure-diffusion case (Figure 2 of the main text). On the other hand, the estimated largeness of Gr inspires considering the limit opposite to the pure-diffusion one, namely that of $Gr \to \infty$ and boundary layers[S9,S10], which is no doubt more pertinent to the present experiments and which we carry out here. At the same time, one should *a priori* recognize that $Gr \sim 852$ is probably not large enough for such a calculation to be more than an advanced estimation. Especially considering that the large parameter entering the boundary-layer scheme (see below) is only as large as $Gr^{1/5} \sim 3.9$. Anyhow, while an exact modelling still awaits its realisation, we shall here stick to a more accessible asymptotic analysis. As it is typically the case, quasi-stationarity is assumed: the drop evaporates much slower than the concentration field is established. Thus, at each instant and for each shape of the drop during the process of evaporation, the concentration and flow fields are assumed to be stationary.

While the temperature dependence is neglected as said above, we do have to take into account the dependence of the dynamic viscosity μ_g of the gas mixture on χ. The following semi-empirical formula is used[S11]:

$$\mu_g = \frac{\mu_v\chi}{\chi + (1 - \chi)\,\Phi_{12}} + \frac{\mu_{\text{air}}\,(1 - \chi)}{\chi\,\Phi_{21} + 1 - \chi},$$

$$\Phi_{12} = \frac{1}{\sqrt{8}}\left(1 + \frac{M_v}{M_{\text{air}}}\right)^{-1/2}\left[1 + \left(\frac{\mu_v}{\mu_{\text{air}}}\right)^{1/2}\left(\frac{M_{\text{air}}}{M_v}\right)^{1/4}\right]^2,$$

$$\Phi_{21} = \frac{1}{\sqrt{8}}\left(1 + \frac{M_{\text{air}}}{M_v}\right)^{-1/2}\left[1 + \left(\frac{\mu_{\text{air}}}{\mu_v}\right)^{1/2}\left(\frac{M_v}{M_{\text{air}}}\right)^{1/4}\right]^2,$$

where we formally treat air as a one-component gas. For the dynamic viscosity μ_v of pure vapour of HFE-7000 required in the above formula, the value given by 3M™ is used, i.e. $\mu_v = 1.09\times10^{-5}\,\text{Pa\,s}$. On the other hand, the diffusion coefficient D_v is taken to be χ-independent[S11], i.e. a constant.

Boundary-Layer Formulation

We now write down the dimensionless boundary-layer formulation for the stationary axisymmetric buoyancy convection below a pendant-drop surface. The cylindrical radial coordinate r, the vertical
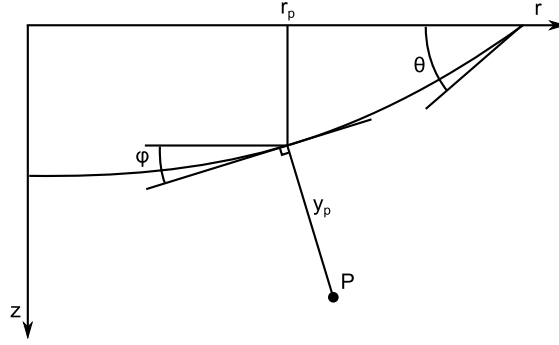
Figure S6: The boundary-layer coordinates r and y of a point P (designated on the sketch as r_{p} and y_{p}).

coordinate z (directed downwards, with $z = 0$ at the solid surface) and the coordinate y (explained below) are all made dimensionless with the contact radius R_c, used as the lengthscale. The drop surface is represented as $z = h(r)$ (for $0 < r < 1$). For the coordinate along the drop surface, we use r with the corresponding metric coefficient $H_r(r) = \sqrt{1 + h'^2}$, the prime hereafter denoting the differentiation with respect to r. In the following formulation, the coordinates of any point P outside the droplet are given by the normal distance y to the droplet interface and the radial coordinate r of the foot of this projection (Figure S6). The local slope of the drop surface is given by the angle $\varphi(r) = -\arctan h'$ with the horizontal, the contact angle being $\theta = \varphi(1)$. Note that $H_r = 1/\cos\varphi$. The tangential and orthogonal (to the drop surface) velocity field components u and v are made dimensionless with ν_{air}/R_c, while the pressure p (deviation from the hydrostatic pressure distribution in the unperturbed, pure air) with $\mu_{\mathrm{air}}\nu_{\mathrm{air}}/R_c^2$. Following the general principles[S9], the sought dimensionless boundary-layer formulation can now be written as (further explanations below)

$$\frac{1}{H_r}\left(\frac{\partial u}{\partial r} + \frac{1}{r}u\right) + \frac{\partial v}{\partial y} = 0\,, \tag{19}$$

$$\tilde{\rho}_g(\chi)\left[\frac{u}{H_r}\frac{\partial u}{\partial r} + \left(v - Sc^{-1}\frac{M_v/M_{\mathrm{air}} - 1}{\tilde{\rho}_g(\chi)}\frac{\partial \chi}{\partial y}\right)\frac{\partial u}{\partial y}\right] = -\frac{1}{H_r}\frac{\partial p}{\partial r} + \frac{\partial}{\partial y}\tilde{\mu}_g(\chi)\frac{\partial u}{\partial y} - Gr\frac{\chi}{\chi_{\mathrm{sat}}(T_{\mathrm{amb}})}\sin\varphi\,, \tag{20}$$

$$0 = -\frac{\partial p}{\partial y} + Gr\frac{\chi}{\chi_{\mathrm{sat}}(T_{\mathrm{amb}})}\cos\varphi\,, \tag{21}$$

$$\frac{u}{H_r}\frac{\partial \chi}{\partial r} + v\frac{\partial \chi}{\partial y} = Sc^{-1}\frac{\partial^2 \chi}{\partial y^2}\,, \tag{22}$$

$$u = u_\sigma\,, \quad v = -\frac{Sc^{-1}}{1-\chi}\frac{\partial \chi}{\partial y}\,, \quad \chi = \chi_\sigma \qquad \text{at} \quad y = 0\,, \tag{23}$$

$$u \to 0\,, \quad p \to 0\,, \quad \chi \to 0 \qquad \text{as} \quad y \to +\infty\,, \tag{24}$$

where Gr is defined according to eq 17 with eq 18, $\tilde{\rho}_g(\chi) = \rho_g(\chi)/\rho_{\mathrm{air}} = 1 + (M_v/M_{\mathrm{air}} - 1)\chi$, and $\tilde{\mu}_g(\chi) = \mu_g(\chi)/\mu_{\mathrm{air}}$.

The problem is here more conveniently formulated in terms of the *mole average velocity*[S11], in contrast with the usual, mass average (or barycentric) one. This is why the continuity equation, eq 19, is merely in the form of the divergence of the velocity field equal to zero, in spite of strong density variations: the mole density c_g is here assumed constant, as discussed above. The same is true for the species conservation equation, eq 22, which adopts a particularly simple form. In fact,

within the leading-order boundary-layer approach to which the present formulation pertains, there is no difference between the two types of velocity as far as the u component is concerned. This is not the case for the v component though. Namely, the mass average orthogonal velocity-field component is given by the term in parentheses on the left-hand side of the tangential momentum equation, eq 20, and so this equation clearly adopts the usual form in terms of the mass average velocity. Note that both tangential (eq 20) and orthogonal (eq 21) buoyancy force components are present in the formulation (see also discussion below). Equation 24 states that three dependent variables (but not v) fade away at the outer edge of the boundary layer.

For the interfacial boundary conditions defined in eq 23, three different variants are considered. In all of them, the condition of the normal velocity determined by evaporation ($y = 0$, eq 23, second relation) remains unchanged. On the other hand, the mole fraction distribution along the drop surface χ_σ (eq 23, third relation) is either taken constant and equal to the saturation mole fraction determined by the ambient temperature or rather adopted from the experimental measurement of the interfacial mole fraction (as explained in the main text). For the surface tangential velocity u_σ (eq 23, first relation) there also are two possibilities. Either we assume it equal to zero (i.e. neglible as compared to the velocities present in the gas) or alternatively, in light of the large temperature drops measured experimentally, we compute the corresponding thermal Marangoni flow inside the droplet and use the resulting u_σ distribution in the gas boundary-layer simulation. These four options lead to only three reasonable cases, which are shown in the main text: constant interfacial temperature (equal to T_{amb} and $\chi_\sigma = \chi_{\mathrm{sat}}(T_{\mathrm{amb}})$) and a stagnant droplet ($u_\sigma = 0$), which is denoted by the subscript Tc in the figures; non-uniform interfacial temperature $T_\sigma(r)$ adopted from experiment and $\chi_\sigma = \chi_{\mathrm{sat}}(T_\sigma)$, but still a stagnant droplet ($u_\sigma = 0$), which is denoted by the subscript Tv; and finally, the same as the latter case but now with u_σ determined from the Marangoni flow inside the droplet associated with $T_\sigma(r)$, which is denoted by the subscript Ma. The details of how this Marangoni flow is calculated are given in the following subsection.

Once the solution of the problem, eqs 19-24, is obtained, the local evaporation flux (mass per unit area and per unit time) at the drop surface is finally expressed as

$$J_l(r) = \frac{P_{\mathrm{amb}}}{\mathcal{R} T_{\mathrm{amb}}} \, M_v \, \frac{\nu_{\mathrm{air}}}{R_c} \, v(r, y = 0) \,, \tag{25}$$

where v is dimensionless as in eqs 19-24. These local evaporation rates are shown in Figure 5 in the main text for the three mentioned cases as $J_{l,Tc}$, $J_{l,Tv}$ and $J_{l,Ma}$.

We note that, well in the spirit of the boundary-layer approach, one may expect that the variables can be rescaled with certain powers of Gr so that Gr disappears from the formulation. However, here such a scaling-out of Gr can be achieved either in the tangential buoyancy term, or in the orthogonal one, but not in both simultaneously. Moreover, the extraneous (with respect to the buoyancy convection) factor of u_σ must be equal to zero to this purpose. For instance, to get rid of Gr in the orthogonal buoyancy term, the following change of variables applies: $u \to Gr^{2/5}u$, $v \to Gr^{1/5}v$, $y \to Gr^{-1/5}y$, $p \to Gr^{4/5}p$ (the other variables not being modified). This leaves a factor of $Gr^{1/5}$ in front of the tangential buoyancy term (instead of Gr in eq 20). In this way we see that, given that the present analysis is valid as $Gr \to \infty$, sufficiently small surface slopes must be implied (such that $Gr^{1/5}\varphi = O(1)$) to have both types of buoyancy contribution at the same leading order. For slopes smaller than that (i.e. for sufficiently flattened pendant drops), it is the orthogonal buoyancy that is prevailing. For larger slopes, it is the tangential buoyancy, as it should in fact be expected.

It is clear from physical considerations that the boundary-layer flow here initiates at the contact

line and is directed towards the symmetry axis (hence $u < 0$). Formally, in the framework of the formulation given by eqs 19-24, it is the orthogonal buoyancy that always (irrespective of the values of Gr and θ) dominates over the tangential one at the initiation. This can e.g. be verified a posteriori using the corresponding initiation solution, which is self-similar:

$$u = -Gr^{2/5}\cos^{1/5}\theta\,(1-r)^{1/5}U(\eta)\,, \quad v = Gr^{1/5}\cos^{3/5}\theta\,(1-r)^{-2/5}V(\eta)\,,$$

$$p = Gr^{4/5}\cos^{2/5}\theta\,(1-r)^{2/5}P(\eta)\,, \quad \chi = X(\eta)\,, \quad \eta = Gr^{1/5}\cos^{3/5}\theta\,y\,(1-r)^{-2/5}\,,$$

valid as $r \to 1$ (note that $H_r = 1/\cos\theta$ at $r = 1$). U, V, P and X satisfy the following boundary-value problem for ordinary differential equations (prime denoting differentiation with respect to η):

$$\frac{1}{5}U - \frac{2}{5}\eta U' + V' = 0\,,$$

$$\tilde{\rho}_g(X)\left[\frac{1}{5}U^2 + \left(V - \frac{2}{5}\eta U - Sc^{-1}\frac{M_v/M_{\text{air}} - 1}{\tilde{\rho}_g(X)}X'\right)U'\right] = -\frac{2}{5}P + \frac{2}{5}\eta P' + (\tilde{\mu}_g(X)U')'\,,$$

$$0 = -P' + \frac{X}{\chi_{\text{sat}}(T_{\text{amb}})}\,,$$

$$\left(V - \frac{2}{5}\eta U\right)X' = Sc^{-1}X''\,,$$

$$U = 0\,, \quad V = -\frac{Sc^{-1}}{1 - X}X'\,, \quad X = \chi_{\text{sat}}(T_{\text{amb}}) \qquad \text{at} \quad \eta = 0\,,$$

$$U \to 0\,, \quad P \to 0\,, \quad X \to 0 \qquad \text{as} \quad \eta \to +\infty\,,$$

which is solved numerically by a shooting method. We see that the behaviour of the solution is here singular at the starting point (as $r \to 1$), which is not atypical at all in the general context of boundary layers[S9]. In particular, the boundary layer develops from a zero thickness, the thickness growing as $(1-r)^{2/5}$. The local evaporation flux diverges as $J_l \propto (1-r)^{-2/5}$ as $r \to 1$ (the same as $v(r, \eta = 0)$, cf. eq 25). This is not a fundamental divergence though (unlike the one in the pure-diffusion case), in the sense that the boundary-layer approach is not valid in a small vicinity of the starting point anyway. The zone where it breaks down can be estimated e.g. by setting $u \sim v$ within the self-similar solution (in the region of validity, it must be $u \gg v$ as $Gr \to \infty$). This leads to an estimation $1 - r = O(Gr^{-1/3})$ for the zone in question. We note that in the case Ma, when $u_\sigma \neq 0$ is considered, u_σ behaves less singularly as $r \to 1$ than the above self-similar solution and thus does not interfere to leading order at the initiation: in fact, with the present fitting of the interfacial temperature from experiment, we have $u_\sigma \propto (1-r)$ as $r \to 1$ (see also the next subsection), whereas $u \propto (1-r)^{1/5}$ for the self-similar solution.

The problem is discretised by finite differences. The conditions at $y \to \infty$ are approximated at some finite $y = y_{\text{max}}$ deemed to be sufficiently large. The initiation solution is applied (for all points along y) at some $r = r_{\text{max}} < 1$ deemed to be sufficiently close to $r = 1$ (the first station in the computation scheme). Here we use $r_{\text{max}} = 0.999$. Then, the solution (for all y) is advanced to the next chosen discrete position (station) in the decreasing sense of r, etc. This step-by-step procedure, involving at each step two sufficiently close neighbouring stations, one at which the solution is already known and the other where it is sought, is here realised similarly to Potter and Riley[S10]. The procedure can in principle be continued up to $r = 0$. Practically, however, it has to be stopped at a small finite value $r = r_{\text{min}}$ (here we go up to $r_{\text{min}} = 0.04$) in view of the

geometrical singularity at the symmetry axis anticipated by the present boundary-layer solution in the form of a corresponding singular behaviour interpreted as a developing eruption precursor as r is decreased[S10]. In the range $0 < r < r_{\min}$, the local flux (eq 25) is then obtained by interpolation to the point $\{r = 0, J_l = 0\}$ in accordance with the expected behaviour in the framework of the leading-order boundary-layer theory[S10]. We note that the boundary-layer approach actually ceases to be valid for a certain interval of r around $r = 0$, whose length is inversely proportional to a small positive power of the Grashof number[S10]. In our case, with $Gr \sim 852$, we estimate that this interval may be as large as $0 < r < 0.5$. Given the earlier mentioned invalidity in a vicinity of $r = 1$, the r range where the boundary-layer computation results can be meaningfully compared with experiment is thus roughly limited in Figure 5 of the main text to $0.5 < r < 0.9$.

Marangoni flow inside the drop

The computation is based upon the full incompressible Navier-Stokes equations with constant material properties and the appropriate boundary conditions. The Marangoni term in the tangential stress balance at the drop interface is evaluated using the interfacial temperature distribution measured in the experiment. Let u and w be the cylindrical radial and vertical velocity-field components, respectively, adimensionalised with ν_l/R_c, where $\nu_l = 3.21 \times 10^{-7}\,\mathrm{m^2/s}$ is the kinematic viscosity of the liquid. Note that here u is different from the previous subsection. The hydrodynamic pressure p is made dimensionless with $\mu_l \nu_l/R_c^2$, where $\mu_l = 0.45 \times 10^{-3}\,\mathrm{Pa\,s}$ is the dynamic viscosity of the liquid. As before, R_c is used as the length scale throughout. The cylindrical coordinates used (r and z) are the same as in the previous subsections. The continuity and momentum equations can be written as

$$\frac{\partial u}{\partial r} + \frac{u}{r} + \frac{\partial w}{\partial z} = 0\,,$$

$$u\frac{\partial u}{\partial r} + w\frac{\partial u}{\partial z} = -\frac{\partial p}{\partial r} + \frac{\partial^2 u}{\partial r^2} + \frac{1}{r}\frac{\partial u}{\partial r} - \frac{u}{r^2} + \frac{\partial^2 u}{\partial z^2}\,,$$

$$u\frac{\partial w}{\partial r} + w\frac{\partial w}{\partial z} = -\frac{\partial p}{\partial z} + \frac{\partial^2 w}{\partial r^2} + \frac{1}{r}\frac{\partial w}{\partial r} + \frac{\partial^2 w}{\partial z^2}\,.$$

The boundary conditions include the no-slip and non-penetration ones at the bottom:

$$u = 0\,, \quad w = 0 \qquad \text{at} \quad z = 0\,,$$

while the non-penetration condition at the droplet interface (the evaporation-induced velocity is neglected versus the Marangoni one) and the tangential stress balance (neglecting the gas shear stress) read

$$w = u\frac{dh}{dr}\,, \quad 2\frac{dh}{dr}\left(\frac{\partial w}{\partial z} - \frac{\partial u}{\partial r}\right) + \left[1 - \left(\frac{dh}{dr}\right)^2\right]\left(\frac{\partial u}{\partial z} + \frac{\partial w}{\partial r}\right) = \frac{d\sigma}{dT}\frac{R_c}{\mu_l \nu_l}\frac{dT_\sigma}{dr}\left[1 + \left(\frac{dh}{dr}\right)^2\right]^{1/2}$$

$$\text{at} \quad z = h(r)\,,$$

where T_σ [K] is the experimentally measured interfacial temperature distribution and $d\sigma/dT = -1.06 \times 10^{-3}\,\mathrm{N/m\,K}$ is the surface tension variation with the temperature. Note that in the Marangoni term (the right-hand side), unlike the rest of the formulation, all the quantities are here dimensional, except for r and h. The normal stress balance is not used as the drop shape,

$z = h(r)$, is considered as prescribed. The symmetry at the axis can be expressed by

$$u = 0\,, \quad \frac{\partial w}{\partial r} = 0\,, \quad \frac{\partial p}{\partial r} = 0 \qquad \text{at} \quad r = 0\,.$$

The behaviour of the solution as $r \to 1$, which can be used for formulating the corresponding boundary conditions, is determined by the associated "corner" solution of the creeping-flow (Stokes) equations. As T_σ is here fitted from experiment such as to possess a finite value of dT_σ/dr as $r \to 1$, one can establish that the velocity field decays proportionally to the distance to the contact line, $u = O(1 - r)$ and $w = O(1 - r)$. In particular, we see that $u \to 0$ and $w \to 0$ as $r \to 1$. On the other hand, the pressure field diverges logarithmically. From the corner solution in question, one can obtain

$$p = -\frac{d\sigma}{dT}\frac{R_c}{\mu_l \nu_l}\frac{dT_\sigma}{dr}\bigg|_{r=1}\frac{\sin\theta\sin 2\theta}{\sin 2\theta - 2\theta\cos 2\theta}\log\left[(1-r)^2 + z^2\right] + \text{const}\,,$$

where $\theta = -\arctan dh/dr\big|_{r=1}$ is the contact angle. Given that the absolute pressure values are immaterial in the present incompressible formulation with a prescribed interface, one can choose $\text{const} = 0$ without loss of generality.

After introducing a new variable $\tilde{z} = z/h(r)$, the problem is discretised with the help of finite differences on a uniform rectangular grid. It is solved by the Newton-Raphson method implemented in Wolfram Mathematica (`FindRoot` command). As a result of this computation, one obtains in particular the tangential velocity u_σ distribution at the drop interface used in eq 23.

Simulation Settings

The above (quasi-stationary) analysis is performed for 11 different instances during the droplet evaporation. The droplet contour and the interfacial temperature are both fitted with smooth analytic functions and the fitting coefficients are shown in Table S1. The contour is fitted to a 4th order polynomial ($z = ar^4 + br^2 + c$) with r, z expressed in pixels (1 pixel here equals 7.4µm). The fitting coefficients used in eq 4 for the interfacial mole fractions (from where the temperature is inferred by means of the Clausius-Clapeyron relation) are α, β and γ.

Table S1: Fitting coefficients used in the simulations.

R_c [mm]	$a \times 10^{-9}$	$b \times 10^{-3}$	c	α	β	γ
2.10	7.46	-2.43	150	0.435	3.54	2.82
2.02	6.79	-2.37	138	0.216	0.82	6.85
1.92	6.81	-2.23	120	0.232	0.84	6.79
1.87	5.68	-2.17	113	0.333	1.54	4.77
1.81	5.25	-2.11	106	0.360	2.22	3.93
1.76	5.03	-2.08	99	0.341	1.64	4.62
1.63	4.60	-1.97	84	0.354	2.12	3.32
1.56	5.08	-1.99	78	0.305	1.32	4.36
1.49	2.01	-1.85	70	0.396	2.77	3.03
1.41	3.73	-1.93	64	0.363	2.12	2.97
1.25	0.14	-1.83	51	0.361	2.40	2.71

In addition to the computation results provided in the main text, some further details are
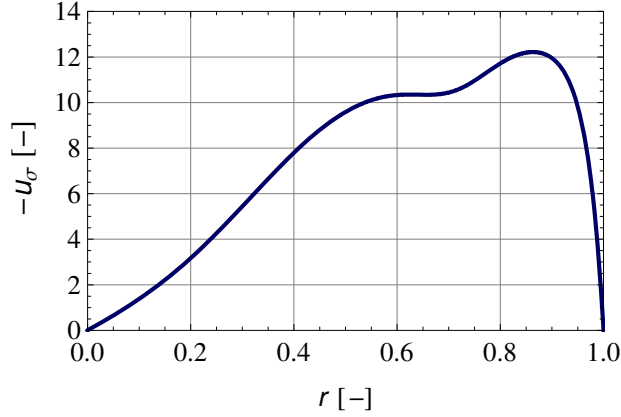
shown in Figures S7 and S8.

Figure S7: Computed tangential surface velocity (adimensionalised with ν_{air}/R_c, as in eq 23) of the Marangoni flow inside the droplet with $R_c = 1.81\,\mathrm{mm}$. Quite a similar single-vortex Marangoni convection has also been obtained elsewhere[S13,S14].
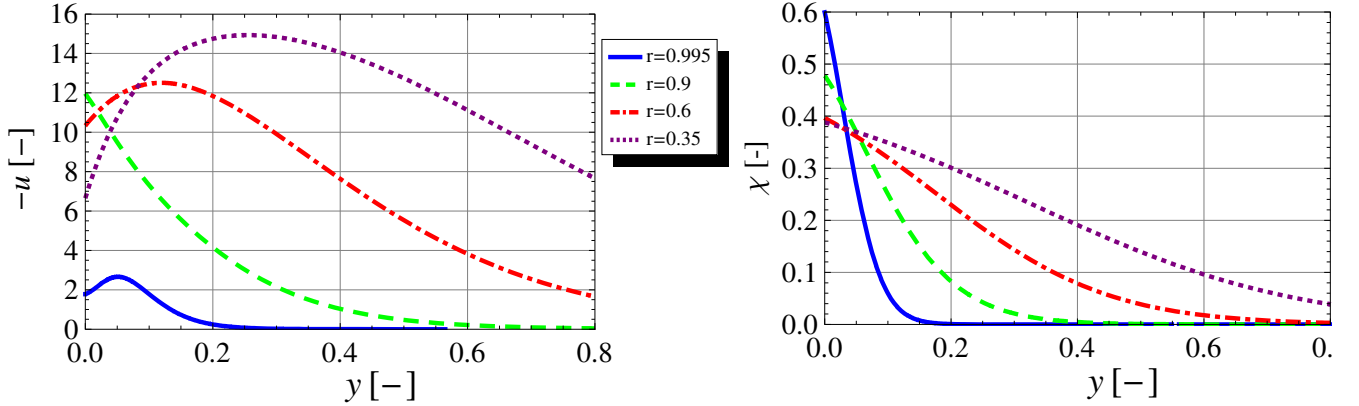

Figure S8: Computed tangential-velocity and mole-fraction orthogonal profiles at various radial positions along the interface (adimensionalised as in eqs 19-24) in the case Ma for the droplet with $R_c = 1.81\,\mathrm{mm}$.

D. Estimation of temperature variations in the wafer

Here we provide estimations confirming our hypothesis that the temperature at the contact line is close enough to the ambient one so as to neglect the difference. The way we proceed is two-fold. On the one hand, we assess the global temperature drop in our silicon wafer due to evaporative cooling. On the other hand, we estimate the temperature non-uniformity in the wafer taking into account a particularly high evaporation flux at the contact line.

The energy required to evaporate a volume V_l of the liquid is $V_l\,\rho_l\,L$, where $\rho_l = 1400\,\mathrm{kg/m^3}$ is the HFE-7000 liquid density and $L = 142\,\mathrm{kJ/kg}$ is its latent heat of evaporation. If this comes at the expense of cooling the wafer, it must be equal to $V_s\,\rho_s\,c_{ps}\,\Delta T$, where ΔT is the wafer temperature drop, V_s the volume of the wafer, ρ_s its density and c_{ps} its specific heat. For silicon,

we take $\rho_s = 2329\,\mathrm{kg/m^3}$ and $c_{ps} = 1414\,\mathrm{J/kgK}$. Our wafer is circular with a radius of $2.54\,\mathrm{cm}$ and a thickness $d_s = 0.5\,\mathrm{mm}$, hence $V_s \approx 1\,\mathrm{ml}$. For our pendant drops, $V_l \sim 5\,\mu\mathrm{l}$. This yields $\Delta T \sim 0.3\,\mathrm{K}$, which is deemed to be inessential. However, in view of a finite thermal diffusivity $\kappa_s = \lambda_s/\rho_s c_{ps}$ of the solid (even though relatively large here, with $\lambda_s = 149\,\mathrm{W/m\,K}$ for silicon), the cooling does not proceed uniformly in the whole wafer, but rather involves distances of the order of $\sqrt{\kappa_s t}$ from the droplet, where t is the time. Thus, the energy lost due to the cooling is $\sim \pi\,(\sqrt{\kappa_s t})^2\,d_s\,\rho_s\,c_{ps}\,\Delta T = \pi\,d_s\,\lambda_s\,\Delta T\,t$. In the beginning, the global evaporation rate is at its maximum, of the order of $J_g \sim 1\,\mu\mathrm{l/s}$ (cf. Figure 6), or in mass units $J_g \sim 1.4 \times 10^{-6}\,\mathrm{kg/s}$. Somewhat overestimating, the evaporation energy up to the moment t is of the order of $J_g\,L\,t$. Equating the two energies, one obtains $\Delta T \sim J_g\,L/(\pi\,\lambda_s\,d_s) \sim 0.9\,\mathrm{K}$, which is already more considerable, but still below $1\,\mathrm{K}$.

Estimation of temperature non-uniformity in the wafer is here somewhat complicated by the fact that neither from experiment nor from modelling we dispose of an exact behaviour of the evaporation flux in a close neighbourhood of the contact line, just where it attains its maximum. To remedy this difficulty, we put to test a number of different reasonable behaviours and show that these result in more or less the same insignificant temperature non-uniformity. Given an estimative character of the analysis, we assume for simplicity that the evaporative heat loss at the drop interface is directly applied/transferred to the surface of the wafer. We focus on the near-contact-line behaviour of the temperature field in the wafer, which is then extrapolated to a distance of the order of the drop radius to yield an estimation of an overall temperature non-uniformity. For definiteness, concrete evaluations are made for a drop with $R_c = 1.81\,\mathrm{mm}$, used as the main illustration example throughout the main text. Note that the wafer thickness, $0.5\,\mathrm{mm}$, is not much smaller than the drop radius, so that the mentioned estimative extrapolation, here made for a semi-infinite substrate, is still deemed to be reasonable. In general, the developments are here similar to Ristenpart et al.[S12].
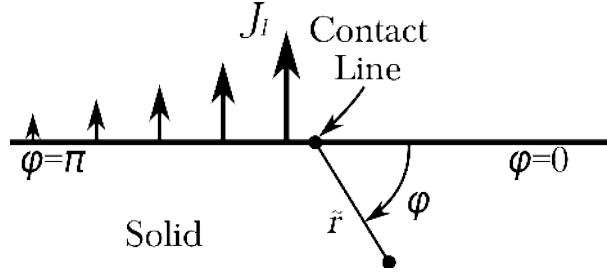

Figure S9: Configuration sketch used for estimation of temperature non-uniformity in the solid in a small vicinity of the contact line.

We use a polar coordinate system $(\tilde{r}, \varphi)$ defined in the meridian cross-section of the drop and centered at the contact line to work in a vicinity of the latter (see Figure S9). The radial coordinate $\tilde{r}$ is adimensionalised with R_c, i.e. $\tilde{r} = [(r - R_c)^2 + z^2]^{1/2}/R_c$. In all test cases used, the local evaporation flux is represented near the contact line ($\tilde{r} \ll 1$) as a power law

$$J_l = J_0/\tilde{r}^{\alpha}\,, \tag{26}$$

with $0 \le \alpha \le 1/2$ and J_0 (kg/m²s) adopted in a reasonable way from either the experiment or the

simulations. The temperature field T_s in the wafer satisfies the Laplace equation

$$\frac{\partial^2 T_s}{\partial \tilde{r}^2} + \frac{1}{\tilde{r}}\frac{\partial T_s}{\partial \tilde{r}} + \frac{1}{\tilde{r}^2}\frac{\partial^2 T_s}{\partial \varphi^2} = 0\,.$$

Let $\varphi = 0$ correspond to the solid–gas surface, where we have an insulation condition due to a poor thermal conductivity of the gas:

$$\partial T_s/\partial \varphi = 0 \qquad \text{at} \quad \varphi = 0\,.$$

The solid–liquid surface corresponds to $\varphi = \pi$, where in accordance with what is said above we impose an evaporative heat loss:

$$\lambda_s \frac{1}{\tilde{r}}\frac{\partial T_s}{\partial \varphi} = -L\,J_l\,R_c \qquad \text{at} \quad \varphi = \pi\,,$$

where $\lambda_s = 149\,\text{W/m\,K}$ is the thermal conductivity of the wafer (silicon in our case) and $L = 142\,\text{kJ/kg}$ is the HFE-7000 latent heat of evaporation. The problem is formulated in the domain $\tilde{r} > 0$, $0 \le \varphi \le \pi$ (see Figure S9).

As a first test case, we use the local evaporation rate in the form applicable to a flattened drop evaporating in the pure diffusion regime, eq 13, even though we rewrite it here with a different factor as follows:

$$J_l = \frac{J_0\sqrt{2}}{\sqrt{1 - r^2/R_c^2}}\,, \tag{27}$$

which conforms to the earlier adopted near-contact-line behaviour, eq 26, with $\alpha = 1/2$. The value of J_0 is taken such that the measured global evaporation flux J_g is equal to the one obtained by the integration of eq 27 over the flattened-drop surface, the latter being $2\pi \int_0^{R_c} J_l\,r\,dr = 2\sqrt{2}\,\pi\,J_0\,R_c^2$. For a HFE-7000 drop with $R_c = 1.81\,\text{mm}$, we have $J_g \approx 0.7\,\mu\text{l/s} \approx 10^{-6}\,\text{kg/s}$ (cf. Figure 6 of the main text) and thus $J_0 \approx 0.034\,\text{kg/m}^2\text{s}$. The appropriate solution of the formulated problem (using eq 26, not eq 27) for T_s with $\alpha = 1/2$ is

$$T_s = T_{s0} + \frac{2LJ_0 R_c}{\lambda_s}\,\tilde{r}^{1/2}\cos\frac{1}{2}\varphi\,,$$

where T_{s0} is a constant (which can in principle be found by matching with the full solution, in the whole wafer). The solution provided is valid in a small vicinity of the contact line. However, extrapolation to $\tilde{r} \sim 1$ (e.g. along $\varphi = 0$) yields an estimate for the spatial variation of the wafer temperature, $\Delta T_s \sim 2LJ_0 R_c/\lambda_s$, on the scale of the droplet radius. With all the parameter values given above, one obtains $\Delta T_s \sim 0.12\,\text{K}$, which is a small value indeed.

As a second test case, we assume the local evaporation rate tending to a finite maximum value at the contact line, and thus $\alpha = 0$ in eq 26. We adopt from experiment (cf. Figure 5 of the main text) $J_0 \sim 0.15\,\text{kg/m}^2\text{s}$. The solution for T_s with $\alpha = 0$ is

$$T_s = T_{s0} + \frac{LJ_0 R_c}{\pi\lambda_s}\,\left(\tilde{r}\varphi\sin\varphi - \tilde{r}\log(\tilde{r}/k)\cos\varphi\right)$$

(k being a constant), and now we see that $\Delta T_s \sim LJ_0 R_c/\pi\lambda_s \sim 0.08\,\text{K}$, once again a small value.

As a last test case, we use the near-contact-line local evaporation rate given by the initiation solution within the boundary-layer scheme (see the corresponding subsection above). In this case,

we have $\alpha = 2/5$ and $J_0 \approx 0.05\,\mathrm{kg/m^2s}$. The solution for T_s with $\alpha = 2/5$ is

$$T_s = T_{s0} + \frac{5LJ_0R_c}{3\lambda_s \sin 3\pi/5}\,\tilde{r}^{3/5}\cos\frac{3}{5}\varphi\,,$$

and now $\Delta T_s \sim 5LJ_0R_c/3\lambda_s \sin 3\pi/5 \sim 0.15\,\mathrm{K}$.

Overall, we see that the cooling of the substrate is here expected to be of the order of $1\,\mathrm{K}$. This is small relative to the temperature fall at the droplet interface (cf. Figure 4), and roughly within the experimental error for the measurement of the interfacial temperature. Thus, we neglect it in the present paper, considering that the substrate (and hence the contact line) are at the ambient temperature.

References

(S1) Dasch, C. One-dimensional tomography: a comparison of Abel, onion-peeling, and filtered backprojection methods. *Applied Optics* **1992**, *31*, 1146–1152.

(S2) Ma, S.; Gao, H.; Wu, L. Modified Fourier-Hankel method based on analysis of errors in Abel inversion using Fourier transform techniques. *Applied Optics* **2008**, *47*, 1350–1357.

(S3) Fagrich, M. E.; Chehouani, H. A simple Abel inversion method of interferometric data for temperature measurement in axisymmetric medium. *Optics and Lasers in Engineering* **2012**, *50*, 336–344.

(S4) Pendrill, L. Refractometry and gas density. *Metrologia* **2004**, *41*, S40–S51.

(S5) Borzsonyi, A.; Heiner, Z.; Kalashnikov, M. P.; Kovacs, A. P.; Osvay, K. Dispersion measurement of inert gases and gas mixtures at 800 nm. *Applied Optics* **2008**, *47*, 4856–4863.

(S6) Popov, Y. Evaporative deposition patterns: Spatial dimensions of the deposit. *Phys. Rev. E* **2005**, *71*, 036313.

(S7) Fuchs, N. *Vaporisation and Droplet Growth in Gaseous Media*; Pergamon Press, **1959**.

(S8) Chauvet, F.; Dehaeck, S.; Colinet, P. Threshold of Bénard-Marangoni instability in drying liquid films. *EPL* **2012**, *99*, 34001.

(S9) Schlichting, H. *Boundary-layer Theory*; McGraw-Hill, **1979**.

(S10) Potter, J.; Riley, N. Free convection from a heated sphere at large Grashof number. *J. Fluid Mech.* **1980**, *100*, 769–783.

(S11) Bird, R.; Steward, W.; Lightfoot, E. *Transport phenomena*; John Wiley & Sons, Inc., **1960**.

(S12) Ristenpart, W. D.; Kim, P. G.; Domingues, C.; Wan, J.; Stone, H. A. Influence of Substrate Conductivity on Circulation Reversal in Evaporating Drops. *Phys. Rev. Lett.* **2007**, *99*, 234502.

(S13) Barash, L. Yu.; T. P. Bigioni, T. P.; V. M. Vinokur, V. M.; Shchur, L. N. Evaporation and fluid dynamics of a sessile drop of capillary size. *Phys. Rev. E* **2009**, *79*, 046301-1–16.

(S14) Barash, L. Yu. Approximate analytical descriptions of the stationary single-vortex Marangoni convection inside an evaporating sessile droplet of capillary size. *arXiv* **2013**, 1308.0342.